



Regenerated cellulose properties tailored for optimized triboelectric output and the effect of counter-tribolayers

Christina Dahlström · Alireza Eivazi · Malin Nejström · Renyun Zhang ·
Torbjörn Pettersson · Haider Iftikhar · Orlando J. Rojas ·
Bruno Medronho · Magnus Norgren

Received: 6 July 2023 / Accepted: 9 January 2024
© The Author(s) 2024

Abstract Cellulose has shown great potential in the development of green triboelectric nanogenerators. Particularly, regenerated cellulose (R-cellulose) has shown remarkably high output power density but the structural features and key parameters that explain such superior performance remain unexplored. In this work, wood cellulose fibers were dissolved in a LiOH(aq)-based solvent to produce a series of R-cellulose films. Regeneration in different alcohols (from methanol to n-pentanol) was performed and the films' structural features and triboelectric performance were assessed. Nonsolvents of increased

hydrophobicity led to R-cellulose films with a more pronounced (1–10) diffraction peak. An open-circuit voltage (V_{OC}) of up to ca. 260 V and a short-circuit current (I_{SC}) of up to ca. 150 μ A were measured for R-cellulose against polytetrafluoroethylene (as negative counter-layer). However, R-cellulose showed an increased V_{OC} of 175% (from 88.1 V) against polydimethylsiloxane when increasing the alcohol hydrocarbon chain length from methanol to n-pentanol. The corresponding I_{SC} and output power also increased by 76% (from 89.9 μ A) and by 382% (from 8.8 W m⁻²), respectively. The higher R-cellulose hydrophilicity, combined with soft counter-tribolayer that follow the surface structures increasing the effective contact area, are the leading reasons for a superior triboelectric performance.

Supplementary Information The online version contains supplementary material available at <https://doi.org/10.1007/s10570-024-05745-8>.

C. Dahlström (✉) · A. Eivazi (✉) · M. Nejström ·
O. J. Rojas · B. Medronho · M. Norgren
Surface and Colloid Engineering, FSCN Research Centre,
Mid Sweden University, Holmgatan 10, 85170 Sundsvall,
Sweden
e-mail: christina.dahlstrom@miun.se

A. Eivazi
e-mail: alireza.eivazi@miun.se

R. Zhang
Material Physics, FSCN Research Centre, Mid Sweden
University, Holmgatan 10, 85170 Sundsvall, Sweden

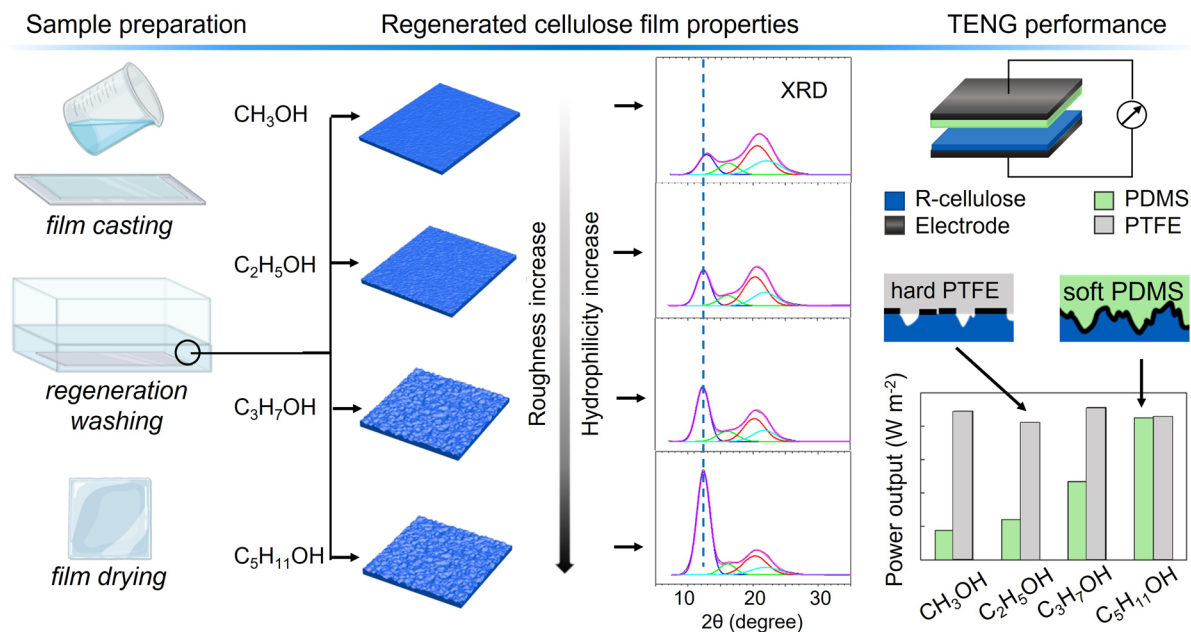
T. Pettersson
Fibre and Polymer Technology, KTH Royal Institute
of Technology, Teknikringen 56-58, 10044 Stockholm,
Sweden

H. Iftikhar · O. J. Rojas
Department of Bioproducts and Biosystems, School
of Chemical Engineering, Aalto University, 00076 Espoo,
Finland

O. J. Rojas
Bioproducts Institute, Department of Chemical
and Biological Engineering, Department of Chemistry,
Department of Wood Science, The University of British
Columbia, Vancouver, BC V6T1Z4, Canada

B. Medronho
MED–Mediterranean Institute for Agriculture,
Environment and Development, CHANGE–Global
Change and Sustainability Institute, Faculdade de Ciências
e Tecnologia, Universidade do Algarve, Campus de
Gambelas, Ed. 8, 8005-139 Faro, Portugal

Graphic abstract



Keywords Regenerated cellulose films · Triboelectricity · Surface structures · E-modulus · Regeneration in alcohol

Abbreviations

TENG	Triboelectric nanogenerator
SEM	Scanning electron microscopy
FE-SEM	Field emission scanning electron microscopy
AFM	Atomic force microscopy
FTIR	Fourier transform infrared spectroscopy
XRD	X-ray diffraction
PTFE	Polytetrafluoroethylene
PDMS	Polydimethylsiloxane
PSD	Power spectral density

Introduction

Triboelectric energy generation has been shown as a promising power-generating technology for sustainable energy harvesting from sources available in our surrounding environments, such as mechanical vibration, water flow and waves, and wind, among others

(Bae et al. 2014; Lee et al. 2019; Wang et al. 2014). The mechanisms behind associated phenomena are triboelectrification and electrostatic induction (Zhou et al. 2020). Essentially, triboelectrification occurs when two different materials achieve physical contact (e.g., sliding or tapping) given the generation of static polarized charges at the interface. Subsequently, static charges accumulate on surfaces separated in air, creating electrical fields that lead to polarization of the electrodes attached to the backside of the materials. If a circuit is constructed between the two electrodes, electrons will move from one electrode to the other due to the difference in electric potential, thereby generating a current. The surface charge density is considered a key factor that determines the performance of triboelectric nanogenerators, TENG (Zi et al. 2015; Zou et al. 2020). Another relevant property that enhances the output performance is a large effective contact area, which depends on the surface structure of the materials, the softness of the surface layers, frequencies, and applied force (Chung and Ke 2020; Kumar et al. 2023; Xu et al. 2020).

The development of TENGs represents an important step towards meeting the increased need for sensors and power electronics. Moreover, TENG design

should ideally involve sustainable or environmentally friendly materials and processes (Zhang et al. 2023; Zhang and Olin 2020). In this regard, widely available cellulose materials play a central role given the regenerative and biodegradable features associated with related structures, which are rich in –OH groups that can be used to tailor the chemical surface composition. Chemical modifications typically do not affect cellulose's bulk features, but rather introduce functional groups to endow highly specific properties (Aziz et al. 2022). Despite the favorable dielectric properties of cellulose, previous reports have mainly focused on fibrous (nonwoven) materials, such as nanocellulose-based films and paper, but their performance in triboelectric generation has not always been so startling. A major breakthrough was recently advanced with our fully “green” TENGs based on regenerated cellulose and commercial cellophane. We found a remarkable output power density of ca. 300 W m⁻², of similar order as that measured for TENGs based on synthetic fluoropolymers (Zhang et al. 2020). Moreover, regenerated cellulose was found to act as a tribopositive layer with a high charge density, +10.05 μC m⁻², which at that time was the most positive material measured and reported in the triboelectric series (Zou et al. 2019).

Cellulose fibers can be extracted from plants and either used as such or in other forms, such as nanocellulose materials or cellulose solutions (Habibi et al. 2010; Medronho and Lindman 2014; Salas et al. 2014; Wågberg et al. 2008). The latter cellulose type involves dissolution processes that are non-trivial: hydrogen bonding and hydrophobic interactions control the solubility of cellulose in a given solvent (Medronho and Lindman 2014, 2015; Medronho et al. 2012). Several solvents have been developed for this purpose, including aqueous-based alkali (NaOH and LiOH), which are of special interest given that they are cost-effective and have a favorable environmental profile. It is intriguing to observe that during the dissolution and coagulation processes, cellulose allomorphy changes from type I to type II (Lindman et al. 2017). In addition, by proper selection of the regeneration conditions, the regenerated cellulose (particularly, regenerated films) can be tuned regarding their crystallinity, surface morphology, transparency, mechanical strength, density, water contact angle, moisture uptake, gas permeability, and dielectric properties

(From et al. 2020; Yang et al. 2011; Yin et al. 2020). However, a fundamental understanding of property-effect relationships and their impact on triboelectric performance of R-cellulose film-based TENGs is far from obvious. Such knowledge is crucial to unveil the underlying mechanisms governing the remarkable triboelectric effect of R-cellulose-based TENGs, and to enable further development and optimization.

In this study, R-cellulose films with tailored structural properties were systematically prepared using cellulose dissolved in cold LiOH/urea(aq) and coagulated in alcohols of different molecular chain length, ranging from methanol to n-pentanol. To test the hypothesis on how the structure, at different length-scales, can affect the triboelectric output, we systematically correlate the properties of the different R-cellulose films induced by the regeneration media (nonsolvent) to their TENG performance. This innovative strategy has not been explored in the past. Hence, we provide relevant insights on the fundamental mechanisms that explain the TENG performance of R-cellulose films.

Materials and methods

Chemicals and materials

The cellulose used for dissolution/regeneration was a commercial dissolving-grade pulp from Domsjö Fabriker Aditya Birla (Örnsköldsvik, Sweden). The weight-average molecular weight (M_w) was 3.2×10^5 g mol⁻¹, and the polydispersity index was 10.3, as determined by size-exclusion chromatography (MoRe Research AB, Sweden). The silicon film used herein was a commercial product under the trade name ELASTOSIL® Film 2030, which was purchased from Wacker Chemie (Germany). The film was made from cross-linked silicone rubber with a thickness of 50 μm, thereafter referred to as PDMS. The PTFE film (130 μm thick) was secured from High-tech-flon®. The copper tape was purchased from Elektrokit. Urea (≥ 99.5%) was purchased from Sigma-Aldrich (Sweden), LiOH·H₂O (56.5%) from Alfa Aesar (Germany), methanol (≥ 99.8%), ethanol (≥ 99.8%), n-propanol (≥ 99%) from VWR Chemicals (Sweden) and n-pentanol (≥ 98%) from Merck (Sweden).

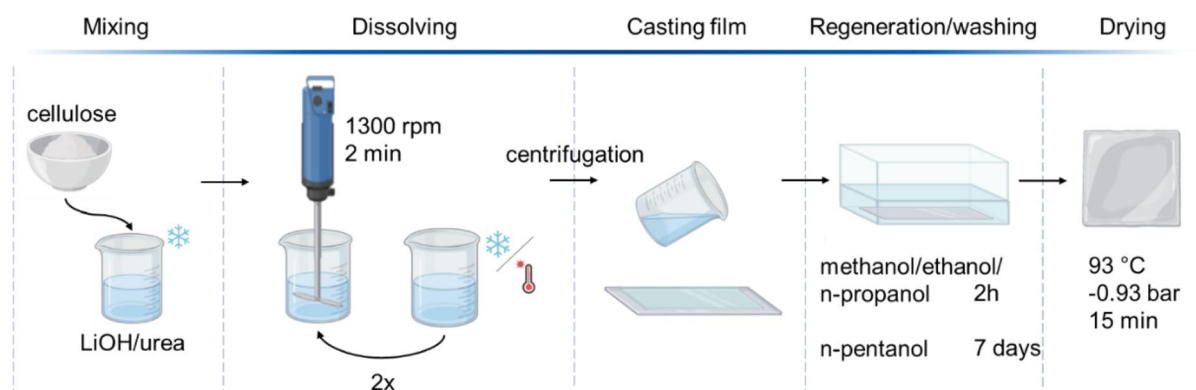


Fig. 1 Schematic illustration of the steps involved in dissolution and regeneration of cellulose fibers to produce the R-cellulose films

Preparation of the cellulose solution

The cellulose fibers were dissolved following the method reported elsewhere (Cai and Zhang 2005; Yang et al. 2019a). In brief, an aqueous solution of 4.6 wt% LiOH and 15 wt% urea was frozen and thawed to $-12\text{ }^{\circ}\text{C}$ and then 4.0 wt% of cellulose pulp was added and stirred with a propeller at 1300 rpm for 2 min. This freeze-thawing-mixing procedure was repeated two additional times to ensure complete dissolution. Finally, the cellulose solution (also known as dope) was centrifugated with a JLA-16.250 fixed angle rotor (Beckman Coulter, USA) at 8000 rpm for 10 min to remove air. The final cellulose solution was clear and no solid particles (e.g., undissolved cellulose fibers) were observed by visual inspection.

Preparation of the R-cellulose films

R-cellulose films were prepared by casting the solution onto glass plates (with a thickness corresponding to the desired thickness in the dry state) and immersed into a regeneration bath filled with the given alcohol type (methanol, ethanol, n-propanol, and n-pentanol). Note that due to the reduced solubility of the $\text{H}_2\text{O}/\text{LiOH}/\text{urea}$ solvent in n-pentanol, the film regenerated in this more hydrophobic alcohol, required a longer regeneration or holding time (168 h) before reaching the equilibrium thickness. For the other, short coagulation alcohols, 2 h was sufficient to attain equilibrium. The films were then placed in a Milli-Q water bath to wash away LiOH and urea, and water was changed daily for three days until reaching a pH value of 7. The films were dried in a Rapid Köthen

(Frank-PTI GMBH, Germany) papermaking system at $93\text{ }^{\circ}\text{C}$ using -0.93 bar for 15 min. The method for dissolving and regenerating the films is schematically shown in Fig. 1. Thickness was measured with a micrometer screw gauge on dry films. The total solids content of the samples was measured by a KERN DBS moisture analyzer and the values were within a narrow range (i.e., $95.7 \pm 0.9\%$). The specific density of all R-cellulose films was $1.36 \pm 0.1\text{ g cm}^{-3}$. The samples were kept sealed in airtight bags until further analysis.

Characterization

Atomic force microscopy

Surface morphology and roughness of the dried films were accessed by atomic force microscopy (AFM; Park Systems NX20, Korea). AFM was operated in non-contact mode in air. A PPP-EFM probe (Park Systems, Korea) with nominal resonance frequency of 75 kHz and force constant 2.8 N m^{-1} was used. AFM images representative areas ($5 \times 5\text{ }\mu\text{m}^2$) on the R-cellulose samples were acquired using a scan rate of 0.3–0.6 Hz. The surface roughness parameter (R_q), mean width of profile elements (RSm) and power spectrum density (PSD) were determined using the Park systems XEI 1.8.5 image analysis software.

The elastic modulus of the samples was acquired based on DMT (Derjaguin-Muller-Toporov) contact model, using Park System's PinPoint™ Nano-mechanical measurement mode. For this purpose, a cantilever with a parabolic tip shape with a radius of 30 nm was used. A SD-R30-NCH probe (Park

Systems, Korea) with the nominal resonance frequency of 330 kHz and force constant of 42 N m⁻¹ was used for both the R-cellulose and PTFE films, while a SD-R30-CONT probe (Park Systems, Korea) with a nominal resonance frequency of 13 kHz and force constant of 0.2 N m⁻¹, was used for the PDMS sample. To measure reliable mechanical properties of the samples, the optical lever sensitivity of the cantilevers was determined on a hard surface (e.g., silicon wafer) together with the out of contact force slope that is used for correction in the algorithm to generate the force vs. separation curves required for the elasticity calculations. Spring constant calibration was performed by the built in Sader and Thermal Tune methods (Hutter and Bechoefer 1993; Sader et al. 1999) for the stiff (SD-R30-NCH, 24.8 N m⁻¹) and the soft (SD-R30-CONT, 0.1 N m⁻¹) cantilevers, respectively. The estimated E-modulus of the films was validated by nanomechanical measurements on identical samples performed in different laboratories using AFM from a different instrument manufacture. The variation in results was estimated to be less than 5% between the facilities.

Scanning electron microscopy

Field emission scanning electron microscopy (FE-SEM) imaging of the R-cellulose films was performed using a TESCAN MAIA3 electron microscope in secondary electron (SE) mode. The cellulose samples were coated with a 2-nm Iridium layer using a Quorum Q150T ES before image acquisition.

Fourier transform infrared spectroscopy

The FTIR spectra of the films were obtained on a Nicolet 6700 spectrometer (Thermo Scientific). All spectra were collected from R-cellulose samples in the region 400–4000 cm⁻¹ with 4 cm⁻¹ resolution and averaged over 32 scans.

X-ray diffraction analysis

X-ray diffraction (XRD) was carried out at room temperature using a Bruker D2 Phaser diffractometer with Cu K α radiation (wavelength 1.54 Å) at 30 kV and 10 mA, in θ –2 θ geometry. The increment was fixed at 0.02°. The cellulose specimens were placed on a silicon single crystal specially cut to provide a low background free from any interfering diffraction peaks. The raw data of XRD analysis for the studied samples and a blank run are provided as separate supplementary data.

Triboelectric measurements

The TENG setup was prepared by attaching the R-cellulose films on a copper tape (acting as electrode) and then fastened on a linear motor as one component, Fig. 2a. The other components, the counter-tribolayers, were fixed on a copper tape and mounted on the linear motor according to the method reported by Zhang et al. (2020). Both, PTFE (130 μ m) and PDMS (50 μ m) films were evaluated as counter-tribolayers. The contact-separation speed of the TENGs was set to 0.3 m s⁻¹. The size of the TENGs was 3 \times 3 cm². Electrical signals were measured with a PXI4071 digital multimeter (National Instruments Corp.).

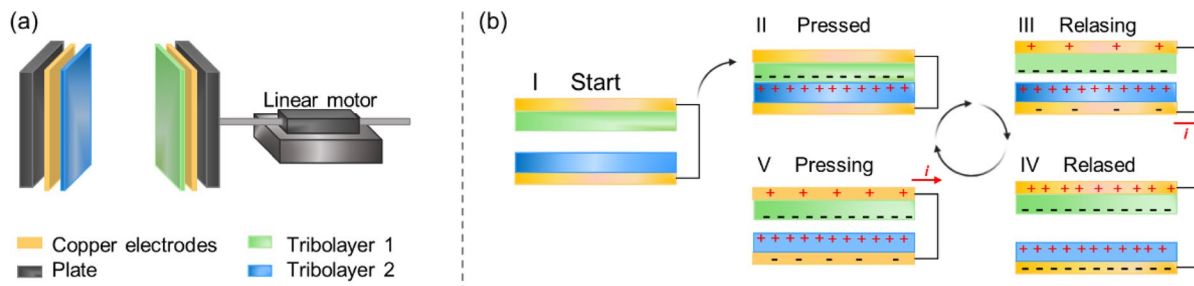


Fig. 2 **a** Schematic illustration of the TENG setup and **b** the working mechanism following contact-separation mode

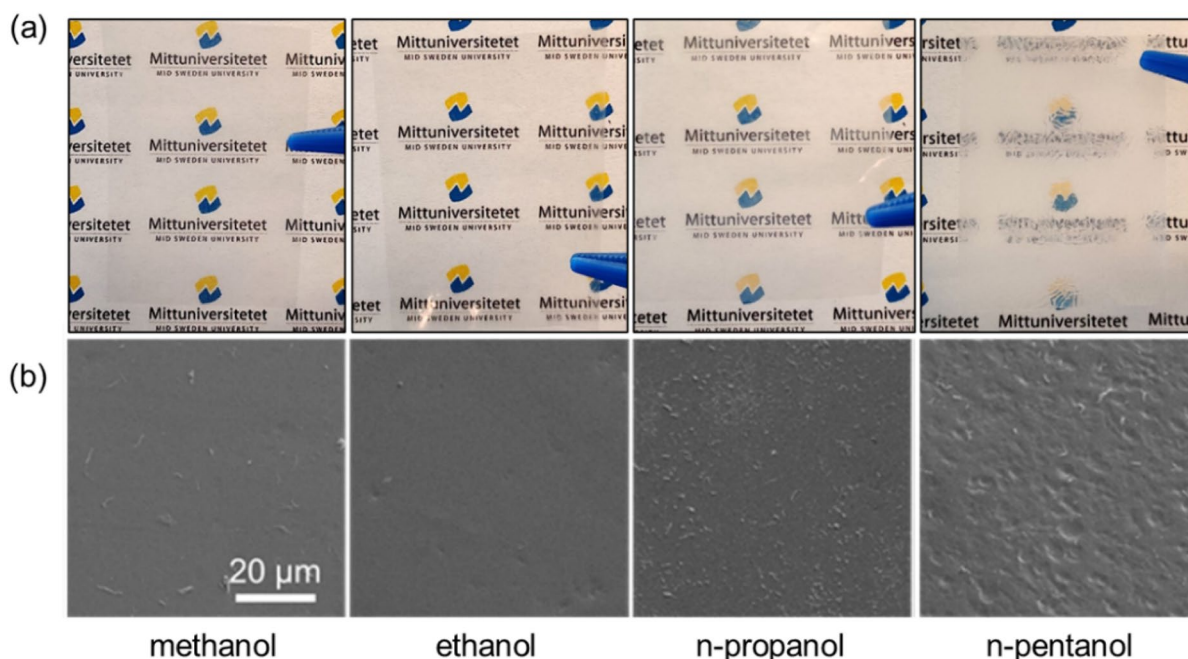


Fig. 3 **a** Photographs of the different regenerated cellulose films placed approximately 2 cm in front of the printed paper in the background. **b** Scanning electron microscopy images of the surface of the sample at 2 000 times magnification. The

films were prepared using different coagulation nonsolvents, from left to right: methanol, ethanol, n-propanol, and n-pentanol

Figure 2b illustrates the working mechanism under the contact-separation mode. At the starting point (I) there are no charges on the tribolayer surfaces. Charge transfer occurs when the two tribolayers are pressed together, into physical contact achieved by the linear motor (II). In the system, R-cellulose donates electrons and becomes positively charged whereas the counter-layer (PDMS or PTFE film) accepts the electrons, becoming negatively charged. When the surfaces are separating (III), the static charges generate an electric field and induce a potential difference between the two electrodes, whereas electrons will flow in the external circuit from one electrode to the other in order to diminish the potential difference, creating a current, until fully released (IV). Following further contacts, when the two layers are pressed into contact again (V), the charges are neutralized and the electrostatic field disappears, resulting in a current flowing in the opposite direction and producing an alternating current.

Results and discussion

Morphological properties of R-cellulose films

Our previous reports highlight that the characteristics of R-cellulose films depend on the miscibility of the aqueous alkali solvent and coagulant (From et al. 2020). However, the film properties and their impact on TENG output remains largely unclear. Therefore, in this work, we go a step further and systematically analyze the effect of nonsolvent in alcoholic baths (i.e., methanol, ethanol, n-propanol and n-pentanol) on the properties of R-cellulose films and evaluation of their correlation with TENG performance. By increasing the chain length of the alcohols, they become less polar and n-pentanol, with the longest hydrocarbon chain length, presents limited water solubility.

Visual inspection of the prepared R-cellulose films reveals that methanol and ethanol-regenerated samples are completely transparent, while coagulation with the less polar alcohols make the films slightly hazy (Fig. 3a). These observations correlate

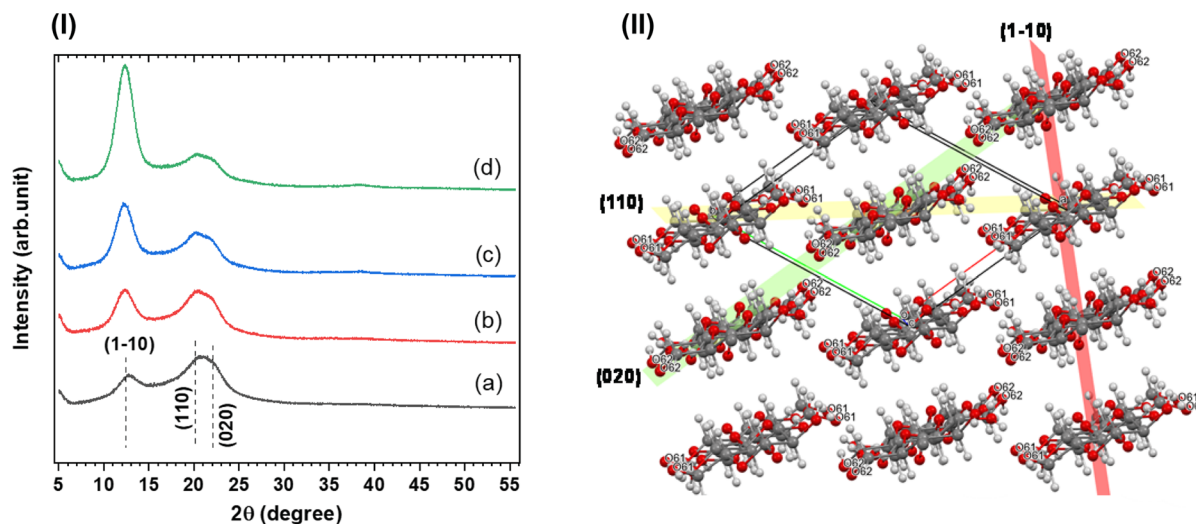


Fig. 4 (I) X-ray diffraction (XRD) patterns of the R-cellulose films prepared by coagulation with **a** methanol, **b** ethanol, **c** n-propanol and **d** n-pentanol. The intensity values were only subtracted from the blank run intensity of the sample holder and presented without applying the smoothing algorithm. The image to the right (II) is the drawing of the crystal structure for cellulose II with (1-10), (110), and (020) planes, as well

as O6 hydroxyl groups. It is constructed with the free Mercury program (Mercury 2022.2.0) developed by the Cambridge Crystallographic Data Center (Macrae et al. 2008) based on the crystal information data for cellulose II, adapted from the work of Langan et al. 2001. The carbon, hydrogen, and oxygen atoms are shown as dark gray, light grey and red balls, respectively

with an increased surface roughness (SEM micrographs, Fig. 3b and AFM 3D height images, Fig. 5). The lower transparency mainly arises from the more pronounced morphological patterns obtained in the films that contribute to light scattering (Hu et al. 2018).

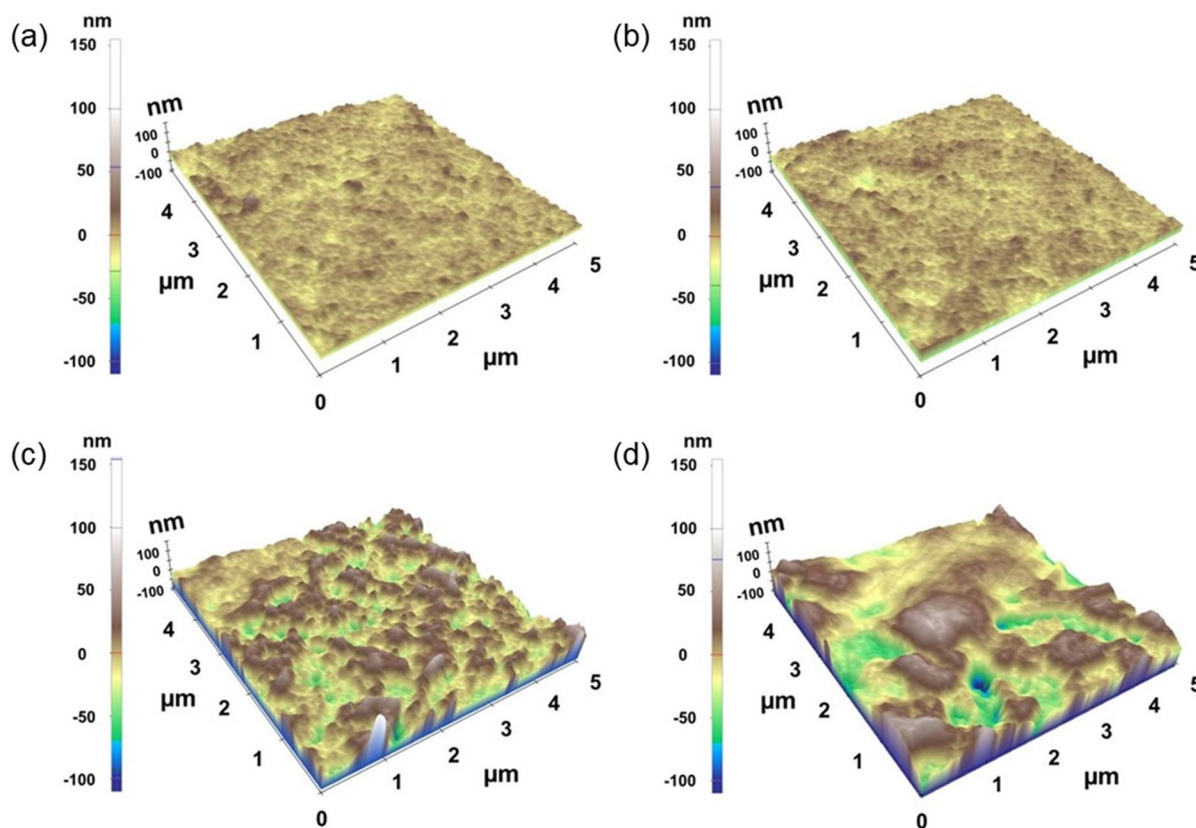
In addition to transparency, other relevant structural properties are presented in Table 1. Regardless of the alcohol used, the dry film thickness is rather similar in ambient conditions. Since there seems to be a direct relationship between the output power and thickness of a polymeric tribolayer, strict control of the thickness of the R-cellulose films is required (Gomes et al. 2018). A regeneration time of 2 h is enough to reach an equilibrium thickness for the short-chain alcohols while the cellulose samples regenerated with the longer alcohol (i.e., n-pentanol) required a prolonged holding time (ca. 7 days). This is due to the low solubility of pentanol in the alkali-based cellulose solvent, and also due to the lower solubility of LiOH and urea in pentanol, which hinders solvent counter-diffusion (i.e., pentanol in the coagulation bath to cellulose and $\text{alkali}_{(\text{aq})}$ from the film to the coagulation non-solvent) and slows down the kinetics of coagulation.

The crystallographic characteristics of R-cellulose films are strongly dependent on the nature of the coagulation bath. As observed in Fig. 4I, the diffractogram peaks for all R-cellulose films are typical of the cellulose II type allomorph. The peaks are located at diffraction angles (2θ) of ca. 12.3, 20.5, and 22°, which correspond to the diffraction of (1-10), (110), and (020) crystallographic plane reflections, respectively (French 2014; Langan et al. 2001). Note: FTIR is also sensitive to the cellulose allomorph (Figure S1 Supplementary Information).

Figure 4 clearly shows that the intensity of (1-10) diffraction peak increases with the alcohol chain length used in the coagulation medium, while the intensity of (110) and (020) diffraction peaks follows the opposite trend. This clearly suggests a significant change in the crystallographic orientation of R-cellulose when the regeneration bath's properties are altered. An important aspect that could cause intensity variations in powder XRD is the preferred orientation (non-random orientations) of the crystallites based on the sample preparation and placement of the sample in the incident X-ray beam. Situations with preferred orientation are particularly common in bacterial cellulose and nanocellulose samples that

Table 1 Properties of the regeneration media and the obtained R-cellulose films

Regeneration liquid	Regeneration time (h)	Solubility of regeneration liquid in water at 20 °C	Thickness (μm)	Surface roughness R_q (nm)	RSm (μm)
Methanol	2	Miscible	24.5 ± 0.8	6.9	0.34
Ethanol	2	Miscible	24.5 ± 0.7	7.1	0.34
n-propanol	2	Miscible	27.1 ± 1.2	20.6	0.59
n-pentanol	168	22 g L^{-1}	28.8 ± 1.0	20.9	1.48

**Fig. 5** Atomic force microscopy (AFM) 3D height images of R-cellulose films prepared by regeneration in alcohols of increasing aliphatic chain length: **a** methanol, **b** ethanol, **c** n-propanol and **d** n-pentanol

once dried at different conditions, which could lead to invalid crystallinity estimation. Regarding the fabricated regenerated cellulose samples developed in this study, the texture analysis by the Rietveld method can shed light on preferred orientation, crystallite size, and fractions of crystalline and amorphous phases in cellulose samples considering the powder XRD data (Salem et al. 2023).

Considering the samples' XRD patterns shown in Fig. 4, similar observations have been reported

regarding the surface and structural properties of cellulose hydrogels prepared from LiOH/urea solvent with various alkyl alcohols (Isobe et al. 2014). In the cited work, the hydrophilicity of the cellulose surface was assigned by probing the surface properties of the cellulose hydrogel via dye (i.e., Congo red) adsorption measurement. They observed that the surface of cellulose hydrogel became less hydrophobic when using alcohols with longer hydrocarbon chains (upon comparing the profiles corresponding to methanol

and butanol nonsolvents), where the intensity of the (1–10) XRD peak is the highest for the sample prepared in butanol. Moreover, the analysis is consistent with the calculation of surface energies of each crystallographic plane (1–10), (110), and (020) of regenerated cellulose (cellulose II), where the (1–10) reflection plane has the highest surface energy, with a value of 178 mN m^{-1} due to many hydroxy groups (Yamane et al. 2006).

The changes in the XRD profiles of R-cellulose prepared with the different alcohols can be further rationalized by the role of cellulose amphiphilicity and controlling phenomena during cellulose regeneration (Lindman et al. 2021). Typically, a set of interconnected phenomena could contribute to the regeneration of cellulose from the studied alkali system and ultimately influence the properties of regenerated cellulose, including regeneration kinetics, various interactions between the components (e.g., cellulose, LiOH, urea, water, and type of alcohols as nonsolvent), solubility, mass transfer and diffusion velocity of the solvent and nonsolvent compounds, which all make the system rather complex. It has been suggested that the regeneration of cellulose from an aqueous alkali-urea system in sodium sulfate solution (forming a hydrated form of cellulose II type allomorph), involves hydrophobic stacking of glucopyranoside rings into monomolecular sheets, reflected in the (110) plane, followed by their mutual association by hydrogen bonding, reflected in the (020) planes (Isobe et al. 2012; Yamane 2015). These observations also apply to the regeneration of cellulose from aqueous solvents as studied by molecular dynamic simulation (Miyamoto et al. 2009). Considering the amphiphilicity of cellulose and involving interactions in the regeneration process, the nonsolvents' polarity (From et al. 2020; Isobe et al. 2011; Kawano et al. 2021) and water solubility (From et al. 2020), were found to be influential in regenerated cellulose structural characteristics and crystallographic orientation. It is reasoned based on the different kinetics of diffusion of solvent components and nonsolvent, which also controls the coagulation rate (From et al. 2020).

In the current study, it is reasonable to assume that a much slower regeneration kinetics of cellulose in the n-pentanol (regeneration in ca. 7 days), having the lower polarity and solubility in the alkali-based cellulose solvent compared to other

short-chain alcohols could give the cellulose chain more time to conform into an ordered structure that is tightly stacked by C-H bonds in axial locations on the glucopyranose rings, a more pronounced (1–10) reflection peak intensity compared to intensity of overlapping peaks of (110) and (020). In this respect, the combination of various techniques (e.g., bulk-averaged and spatially-resolved analytical tools) with the aid of computational analysis would be highly beneficial for understanding changes in the structure of regenerated cellulose induced by coagulation conditions and underlying mechanisms.

As discussed in Fig. 3, the surface roughness increases with the alcohol's chain length. A closer inspection of the SEM images reveals that R-cellulose films regenerated in methanol and ethanol have the smoothest and most homogenous surfaces. This is confirmed by the AFM analyses (Fig. 5) and the extracted R_q roughness, Table 1. R_q is rather similar and lower for the films regenerated in methanol and ethanol (i.e., 6.9 and 7.1 nm, respectively), while the n-propanol and n-pentanol have a R_q value that is approximately three times higher (i.e., 20.6 and 20.9 nm, respectively). Even though the two latter samples have higher and similar roughness, the character of the surface profiles differs, with the n-pentanol regenerated sample having a higher contribution to its roughness coming from larger length scale (PSD in Supplementary Information Figure S2d). The RSm values in Table 1 also shows that n-pentanol has a higher mean width of the surface profile elements compared to the other samples. The surface line profiles of the regenerated cellulose samples are visualized in Supplementary Information Figure S3.

Note that AFM and SEM results only show the small-scale structure at the nano- and micrometer scales. However, since the TENG working principle in the vertical contact mode requires an applied pressure, it is reasonable to assume that large scale roughness e.g., waviness, is of less importance regarding tribo-contact mechanics. The AFM 2D height images of R-cellulose films are presented in Supplementary Information (Figure S4) and AFM 3D height images of the counter-tribolayers (PDMS and PTFE) along with their power spectral density (PSD) are shown in Supplementary Information Figure S2.

Micromechanical properties

The elastic modulus (E-modulus) of the tribolayers is expected to influence the TENGs performance. It has been suggested that polymers with lower moduli generate more charges during triboelectrification (Li et al. 2021). The effect of E-modulus on the TENG performance has been discussed based on the cohesive energy of the materials and the effective contact area (Li et al. 2021; Liu et al. 2020; Šutka et al. 2019; Xi et al. 2021; Yang et al. 2019b). Therefore, the E-modulus of the R-cellulose films and two different counter-tribolayers, PTFE and PDMS, were determined by AFM force spectroscopy (Fig. 6). The so called “violin plots” were used to visualize the distribution of measured values based on the Kernel function. The box plot inside the violin reflects the results’ summary statistics, including the median value, the 25th and 75th percentile of data as the box, and the 5th and 95th percentile of the data as a whisker.

As seen in Fig. 6a, depending on the alcohol type used, the distribution of measured E-modulus values for each R-cellulose sample shows slight differences in the homogeneity of the samples’ nanomechanical characteristics. Such minor differences can be related to various features, such as the inhomogeneous distribution of amorphous and crystalline regions in each prepared R-cellulose sample. The median values determined for the E-modulus of R-cellulose prepared in methanol, ethanol, n-propanol, and n-pentanol were ca. 4.18, 4.51, 3.89, and 5.01

GPa, respectively. The R-cellulose prepared in n-pentanol displays the highest E-modulus; about 10% higher compared to that of samples prepared with ethanol and 20% higher than that of the samples prepared in n-propanol and methanol. The E-modulus of the PTFE and PDMS revealed rather homogenous nanomechanical characteristics (Fig. 6b–c). The median E-modulus values for PTFE and PDMS was ca. 0.510 and 0.002 GPa, respectively, in agreement with literature (Fitzgerald et al. 2019; Šutka et al. 2019).

Triboelectric performance of R-cellulose films

So far, we have analyzed how alcohols of different carbon length affect the microstructural and micromechanical properties of R-cellulose films. In this section, the triboelectric performance is evaluated for two different counter-tribolayers, PTFE and PDMS. PTFE is one of the most commonly used tribolayer materials due to its high negative surface charge density and is therefore included in this study. PDMS is slightly less negative than PTFE but is used for comparison with PTFE due to its softness. In Fig. 7, the open-circuit voltage (V_{OC}), short-circuit current (I_{SC}) and power density are presented for the different TENG setups (note that graphical representations of the V_{OC} and I_{SC} , and surface charge densities for all samples measured with both PTFE and PDMS, are reported in Supplementary Information, Figures S6–S14 and Table S1). A first striking observation is the

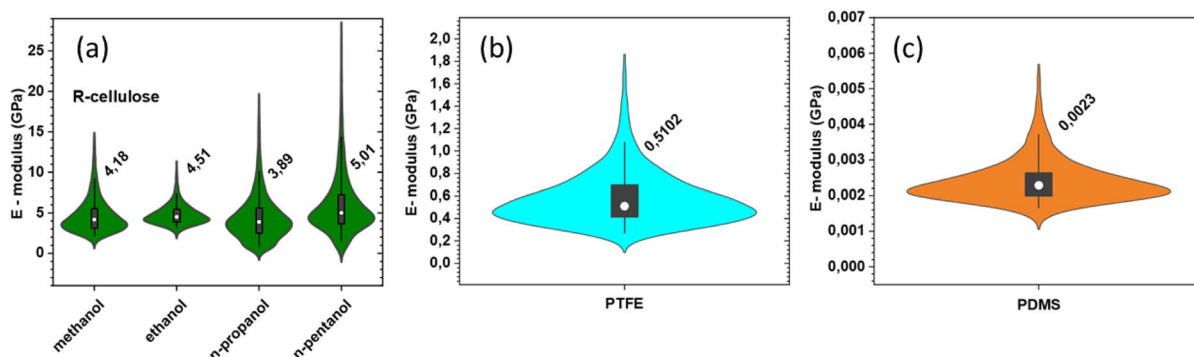


Fig. 6 E-modulus estimated using the DMT (Derjaguin-Muller-Toporov) contact model using AFM force spectroscopy. Violin with boxplots of the data (~16,000 data points) for **a** R-cellulose films prepared in methanol, ethanol, n-propanol, and n-pentanol. **b** PTFE sample and **c** ~13,000 datapoints for

the PDMS sample. Box represents the median (o) and 25/75 percentile, and whiskers represent 5/95 percentile. The median values of elastic modulus for the samples are inserted as numbers on the right-hand side of the violin shape in the plots

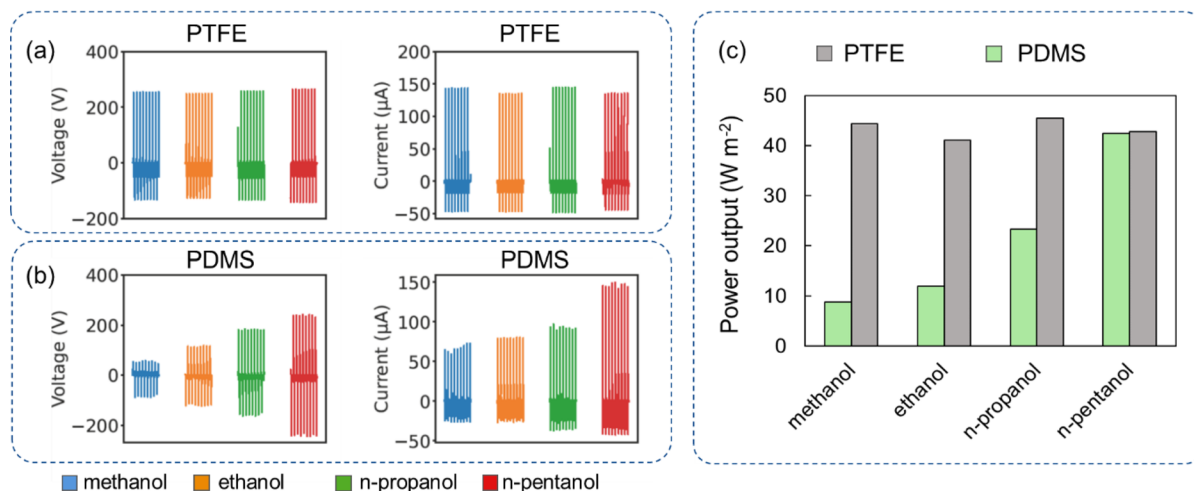


Fig. 7 **a** Open-circuit voltage and short-circuit current measured on the TENGs using PTFE as counter-tribolayer. **b** Open-circuit voltage and short-circuit current measured on

the TENGs using PDMS as counter-tribolayer. **c** Output power density of the TENGs for both PTFE and PDMS as counter-tribolayers

obvious difference between PDMS and PTFE, with the latter presenting higher and rather constant V_{OC} , I_{SC} and output power. The results are in agreement with the triboelectric series presented by Zou et al. (2019), who found that PTFE has a significantly higher negative triboelectric charge density compared to PDMS. Therefore, a superior triboelectric performance is anticipated for PTFE-based TENGs. However, it was surprising that no effect from the R-cellulose different properties were reflected on the triboelectric output using PTFE as the counter tribolayer. For the PDMS, on the other hand, the triboelectric properties are enhanced with increasing the alcohols hydrocarbon chain length used in the regeneration of cellulose. Remarkably, the cellulose sample regenerated in n-pentanol shows an increased output power, more than 380% compared to the cellulose film regenerated with methanol, reaching the level of the PTFE counter-layer.

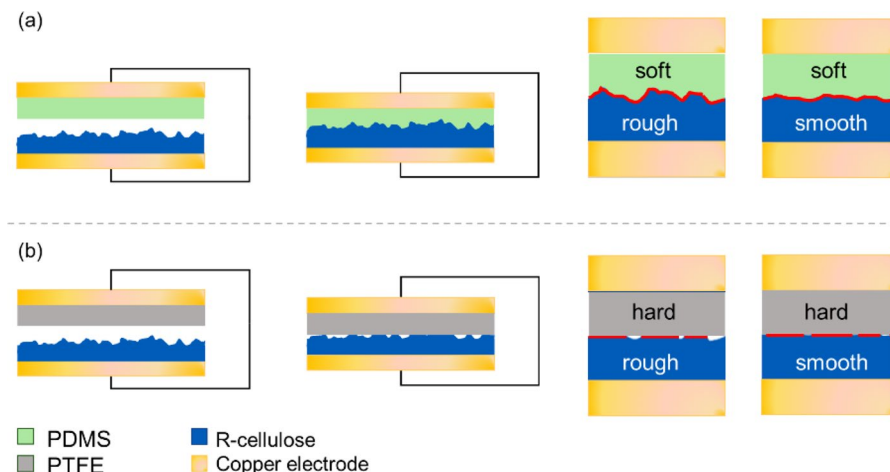
Interestingly, the films regenerated in n-pentanol display 80% higher output power than the ones prepared in n-propanol, even if they have similar roughness and thickness. However, as previously described, the n-pentanol regenerated sample has a different surface profile and length scale of its roughness components compared to n-propanol which might be of importance. Fan et al. (2012) studied the effect of different surface patterns and the size of the patterns in relation to the triboelectric properties and found a

significant improvement for certain structures, but no difference between pattern sizes from 10 μm down to 5 μm .

A deeper analysis of the XRD measurements (Fig. 4) reveals that the (1–10) peak intensity increases with the increasing length of the alcohol chain. This is related to the hydrophilicity of the regenerated cellulose material, i.e., more hydroxyl groups are oriented outwards. It is known that increasing the number density of hydroxyl groups boosts the dielectric constant of a polymer material and, consequently, also its triboelectric output (Lee et al. 2006; Yin et al. 2020). Moreover, the measured E-modulus value of the sample prepared in n-pentanol was almost 20% higher than for that prepared with the n-propanol coagulant.

Overall, it is reasonable to assume that the higher triboelectric performance of TENGs based on n-pentanol regenerated cellulose is related to a higher dielectric constant of the corresponding film. A relevant factor to consider is also the softness of the materials, for instance, the PTFE and PDMS counter-layers, which have significantly different E-moduli (PDMS is “soft” while PTFE is “hard”). The schematic representation in Fig. 8a–b illustrates that a rougher surface has a significantly higher effective contact area with the opposite tribolayer, if the counter-layer is soft. A larger effective contact area generates a higher surface charge density, and thus a higher output voltage

Fig. 8 **a** Schematic drawing of the set-up in which soft PDMS was used as tribolayer to generate electricity with rough and smooth R-cellulose film and **b** hard PTFE was used as tribolayer to generate electricity with rough and smooth R-cellulose film. The red line illustrates the effective contact area



and current (Kumar et al. 2023). Kim et al. (2017) found a correlation between the triboelectric output power and the Young's modulus of the PDMS tribolayer due to the effective contact area, and Xiao et al. (2008) reported that the soft texture of silicone rubber against the hard copper improved transferred charges and output voltage due to better contact. This may further explain the increasing V_{OC} , I_{SC} and power density observed in the PDMS-based TENG setups. The ability for the soft PDMS to deform and adjust to the R-cellulose surface during the fast contact in the TENG measurements might be limited to the μm roughness. Since the propanol regenerated sample has a higher fraction of roughness coming from sub μm length scale compared to the n-pentanol, this would have been translated into a significant higher power output if the PDMS would have managed to get in full contact (see Supplementary Information Fig. S5). A hard and stiff counter-layer is less sensitive to roughness and has a limited ability to engage topographically with the surface of R-cellulose films (the effective contact area will not exceed the contact area of a flat surface).

A further consideration for formal evaluation of R-cellulose films should consider the effect of the coagulating solvent under the framework of the solubility parameter and the extent of swelling, as shown in our earlier work related to filament regeneration (Tripathi et al. 2018, 2019).

Conclusions

Alkali-urea dissolved cellulose was regenerated in a series of coagulants, linear alcohols of increasing aliphatic chain lengths. The effect on the triboelectric properties was evaluated, where alcohols with low water miscibility (higher hydrophobicity) induced the formation of R-cellulose films with enhanced intensity of the (1–10) peak suggesting a higher number of hydroxyl groups pointing outwards and, consequently, a larger dielectric constant of the R-cellulose films is expected.

The R-cellulose films regenerated with the different alcohols displayed similar thickness, but the surface roughness was higher for n-propanol and n-pentanol. However, the triboelectric output power increased by ca. 380% for methanol to n-pentanol using the PDMS as the counter-tribolayer. Thus, roughness is not the only property relevant to the triboelectric performance since material softness is found to also influence the output. The soft PDMS tribolayers engage and capture the inherent roughness of the R-cellulose film more efficiently, resulting in an increased effective contact area and consequently a higher triboelectric output. On the other hand, the effective contact area of the stiff PTFE film is rather constant and similar to the contact area of a flat surface. Nevertheless, the triboelectric output is higher for PTFE, which is anticipated due to its position in the triboelectric series (i.e., higher negative triboelectric charge density than PDMS). Future work will systematically tune and test the dielectric properties.

We identify the critical role of surface structure and crystallographic orientation in the triboelectric effects of R-cellulose films. This satisfies the initial hypothesis that cellulose's structural features are effectively controlling the triboelectric performance. We believe this work paves the way towards the future development of novel cellulose films with enhanced properties and as superior triboelectric materials in a new generation of “green” TENGs.

Acknowledgements This research has been supported by Tresearch. The authors are grateful to Dr. Alfred D. French for his valuable comments and profound discussions related to the XRD analysis.

Author contributions CD, AE and MN conceptualization and methodology. CD, AE, MN and RZ performed experimental work, and TP validated results. CD, AE, RZ and MN prepared the original draft. All authors reviewed and edited the manuscript.

Funding Open access funding provided by Mid Sweden University. The authors are grateful for the financial support from the KK Foundation European Regional Development Fund, the Energy Agency of Sweden, Region Västernorrland, Sundsvall Municipality, Timrå Municipality and Härnösand Municipality. MN acknowledges support from the Swedish Research Council Grant Number 2022–04425. AE acknowledges the financial support from FORMAS grant number 2023–0901. OJR and HI are also grateful for the support received from the ERC Advanced Grant Agreement No 788489 (“BioElCell”) and The Canada Excellence Research Chair initiative (CERC-2018-00006) as well as Canada Foundation for Innovation (Project number 38623). BM acknowledges the Portuguese Foundation for Science and Technology, FCT, through the researcher grant CEECIND/01014/2018 (10.54499/CEECIND/01014/2018/CP1540/CT0002).

Data availability The datasets used or analyzed during the current study are available from the corresponding author on reasonable request.

Declarations

Conflict of interest The authors declare no competing interests.

Consent for publication All authors have given their consent for publication and there is no conflict of interest among all authors.

Open Access This article is licensed under a Creative Commons Attribution 4.0 International License, which permits use, sharing, adaptation, distribution and reproduction in any medium or format, as long as you give appropriate credit to the original author(s) and the source, provide a link to the Creative Commons licence, and indicate if changes were made. The images or other third party material in this article are included

in the article's Creative Commons licence, unless indicated otherwise in a credit line to the material. If material is not included in the article's Creative Commons licence and your intended use is not permitted by statutory regulation or exceeds the permitted use, you will need to obtain permission directly from the copyright holder. To view a copy of this licence, visit <http://creativecommons.org/licenses/by/4.0/>.

References

- Aziz T, Farid A, Fazal H, Kiran M, Ullah A, Zhang K, Li C, Ghazanfar S, Sun H, Ullah R, Ali A, Muzammal M, Shah M, Akhtar N, Selim S, Hagagy N, Samy M, Al Jaouni SK (2022) A review on the modification of cellulose and its applications. *Polymers* 14:1–34. <https://doi.org/10.3390/polym14153206>
- Bae J, Lee J, Kim S, Ha J, Lee B-S, Park Y, Choong C, Kim J-B, Wang ZL, Kim H-Y, Park J-J, Chung U-I (2014) Flutter-driven triboelectrification for harvesting wind energy. *Nat Commun* 5:4929. <https://doi.org/10.1038/ncomm55929>
- Cai J, Zhang L (2005) Rapid dissolution of cellulose in LiOH/urea and NaOH/urea aqueous solutions. *Macromol Biosci* 5:539. <https://doi.org/10.1002/mabi.200400222>
- Chung CK, Ke KH (2020) High contact surface area enhanced Al/PDMS triboelectric nanogenerator using novel overlapped microneedle arrays and its application to lighting and self-powered devices. *Appl Surf Sci* 508:145310. <https://doi.org/10.1016/j.apsusc.2020.145310>
- Fan F-R, Lin L, Zhu G, Wu W, Zhang R, Wang ZL (2012) Transparent triboelectric nanogenerators and self-powered pressure sensors based on micropatterned plastic films. *Nano Lett* 12:3109–3114. <https://doi.org/10.1021/nl300988z>
- Fitzgerald ML, Tsai S, Bellan LM, Sappington R, Xu Y, Li D (2019) The relationship between the Young's modulus and dry etching rate of polydimethylsiloxane (PDMS). *Biomed Microdevices* 21:1–8. <https://doi.org/10.1007/s10544-019-0379-8>
- French AD (2014) Idealized powder diffraction patterns for cellulose polymorphs. *Cellulose* 21:885–896. <https://doi.org/10.1007/s10570-013-0030-4>
- From M, Larsson PT, Andreasson B, Medronho B, Svanedal I, Edlund H, Norgren M (2020) Tuning the properties of regenerated cellulose: effects of polarity and water solubility of the coagulation medium. *Carbohydr Polym* 236:116068. <https://doi.org/10.1016/j.carbpol.2020.116068>
- Gomes A, Rodrigues C, Pereira AM, Ventura J (2018) Influence of thickness and contact area on the performance of PDMS-based triboelectric nanogenerators. *arXiv Preprint arXiv: https://doi.org/10.48550/arXiv.1803.10070*
- Habibi Y, Lucia LA, Rojas OJ (2010) Cellulose nanocrystals: chemistry self-assembly and applications. *Chem Rev* 110:3479–3500. <https://doi.org/10.1021/cr900339w>
- Hu W, Chen G, Liu Y, Liu Y, Li B, Fang Z (2018) Transparent and hazy all-cellulose composite films with superior mechanical properties. *ACS Sustain Chem Eng* 6:6974–6980. <https://doi.org/10.1021/acssuschemeng.8b00814>

- Hutter JL, Bechoefer J (1993) Calibration of atomic-force microscope tips. *Rev Sci Instrum* 64:1868. <https://doi.org/10.1063/1.1143970>
- Isobe N, Kim U-J, Kimura S, Wada M, Kuga S (2011) Internal surface polarity of regenerated cellulose gel depends on the species used as coagulant. *J Colloid Interface Sci* 359:194–201. <https://doi.org/10.1016/j.jcis.2011.03.038>
- Isobe N, Kimura S, Wada M, Kuga S (2012) Mechanism of cellulose gelation from aqueous alkali-urea solution. *Carbohydr Polym* 89:1298–1300. <https://doi.org/10.1016/j.carbpol.2012.03.023>
- Isobe N, Nishiyama Y, Kimura S, Wada M, Kuga S (2014) Origin of hydrophilicity of cellulose hydrogel from aqueous LiOH/urea solvent coagulated with alkyl alcohols. *Cellulose* 21:1043–1050. <https://doi.org/10.1007/s10570-013-0080-7>
- Kawano T, Iikubo S, Andou Y (2021) The relationship between crystal structure and mechanical performance for fabrication of regenerated cellulose film through coagulation conditions. *Polymers* 13:4450. <https://doi.org/10.3390/polym13244450>
- Kim D, Tcho I-W, Jin IK, Park S-J, Jeon S-B, Kim W-G, Cho H-S, Lee H-S, Jeoung SC, Choi Y-K (2017) Direct-laser-patterned friction layer for the output enhancement of a triboelectric nanogenerator. *Nano Energy* 35:379–386. <https://doi.org/10.1016/j.nanoen.2017.04.013>
- Kumar C, Perris J, Bairagi S, Min G, Xu Y, Gadegaard N, Mulvihill DM (2023) Multiscale in-situ quantification of the role of surface roughness and contact area using a novel Mica-PVS triboelectric nanogenerator. *Nano Energy* 107:108122. <https://doi.org/10.1016/j.nanoen.2022.108122>
- Langan P, Nishiyama Y, Chanzy H (2001) X-ray structure of mercerized cellulose II at 1 Å resolution. *Biomacromol* 2:410–416. <https://doi.org/10.1021/bm005612q>
- Lee S, Koo B, Shin J, Lee E, Park H, Kim H (2006) Effects of hydroxyl groups in polymeric dielectrics on organic transistor performance. *Appl Phys Lett* 88:162109. <https://doi.org/10.1063/1.2196475>
- Lee JH, Kim S, Kim TY, Khan U, Kim S-W (2019) Water droplet-driven triboelectric nanogenerator with superhydrophobic surfaces. *Nano Energy* 58:579–584. <https://doi.org/10.1016/j.nanoen.2019.01.078>
- Li J, Shepelin NA, Sherrell PC, Ellis AV (2021) Poly(dimethylsiloxane) for triboelectricity: from mechanisms to practical strategies. *Chem Mater* 33:4304–4327. <https://doi.org/10.1021/acs.chemmater.1c01275>
- Lindman B, Medronho B, Costa C, Alves L, Edlund H, Norgren M (2017) The relevance of cellulose structural features and interactions on dissolution regeneration gelation and plasticization phenomena. *Phys Chem Chem Phys* 19:23704–23718. <https://doi.org/10.1039/C7CP02409F>
- Lindman B, Medronho B, Alves L, Norgren M, Nordenskiöld L (2021) Hydrophobic interactions control the self-assembly of DNA and cellulose. *Q Rev Biophys* 54:e3. <https://doi.org/10.1017/S0033583521000019>
- Liu Y, Liu W, Wang Z, He W, Tang Q, Xi Y, Wang X, Guo H, Hu C (2020) Quantifying contact status and the air-breakdown model of charge-excitation triboelectric nanogenerators to maximize charge density. *Nat Commun* 11:1–8. <https://doi.org/10.1038/s41467-020-15368-9>
- Macrae CF, Bruno IJ, Chisholm JA, Edgington PR, McCabe P, Pidcock E, Rodriguez-Monge L, Taylor R, Streek JV, Wood PA (2008) Mercury CSD 2.0—new features for the visualization and investigation of crystal structures. *J Appl Crystallogr* 41:466–470. <https://doi.org/10.1107/S0021889807067908>
- Medronho B, Romano A, Miguel MG, Stigsson L, Lindman B (2012) Rationalizing cellulose (in)solubility: reviewing basic physicochemical aspects and role of hydrophobic interactions. *Cellulose* 19:581–587. <https://doi.org/10.1007/s10570-011-9644-6>
- Medronho B, Lindman B (2014) Competing forces during cellulose dissolution: from solvents to mechanisms. *Curr Opin Colloid Interface Sci* 19:32–40. <https://doi.org/10.1016/j.cocis.2013.12.001>
- Medronho B, Lindman B (2015) Brief overview on cellulose dissolution/regeneration interactions and mechanisms. *Adv Colloid Interface Sci* 222:502–508. <https://doi.org/10.1016/j.cis.2014.05.004>
- Miyamoto H, Umemura M, Aoyagi T, Yamane C, Ueda K, Takahashi K (2009) Structural reorganization of molecular sheets derived from cellulose II by molecular dynamics simulations. *Carbohydr Res* 344:1085–1094. <https://doi.org/10.1016/j.carres.2009.03.014>
- Sader JE, Chon JWM, Mulvaney P (1999) Calibration of rectangular atomic force microscope cantilevers. *Rev Sci Instrum* 70:3967. <https://doi.org/10.1063/1.1150021>
- Salas C, Nypelö T, Rodriguez-Abreu C, Rojas OJ (2014) Nanocellulose properties and applications in colloids and interfaces. *Curr Opin Colloid Interface Sci* 19:383–396. <https://doi.org/10.1016/j.cocis.2014.10.003>
- Salem KS, Kaser NK, Rahman MA, Jameel H, Habibi Y, Eichhorn SJ, French AD, Pal L, Lucia LA (2023) Comparison and assessment of methods for cellulose crystallinity determination. *Chem Soc Rev* 52:6417–6446. <https://doi.org/10.1039/D2CS00569G>
- Šutka A, Mālnieks K, Lapčinskis L, Kaufelde P, Linarts A, Bērziņa A, Zābels R, Jurkāns V, Gornevs I, Blūms J, Kņite M (2019) The role of intermolecular forces in contact electrification on polymer surfaces and triboelectric nanogenerators. *Energy Environ Sci* 12:2417–2421. <https://doi.org/10.1039/C9EE01078E>
- Tripathi A, Parsons GN, Khan SA, Rojas OJ (2018) Synthesis of organic aerogels with tailorable morphology and strength by controlled solvent swelling following Hansen solubility. *Sci Rep* 8:2106. <https://doi.org/10.1038/s41598-018-19720-4>
- Tripathi A, Rutkevičius M, Bose A, Rojas OJ, Khan SA (2019) Experimental and predictive description of the morphology of wet-spun fibers. *ACS Appl Polym Mater* 16:1280–1290. <https://doi.org/10.1021/acsapm.9b00089>
- Wågberg L, Decher G, Norgren M, Lindström T, Ankerfors M, Axnäs K (2008) The build-up of polyelectrolyte multilayers of microfibrillated cellulose (MFC) and cationic polyelectrolytes. *Langmuir* 24:784–795. <https://doi.org/10.1021/la702481v>
- Wang S, Niu S, Yang J, Lin L, Wang ZL (2014) Quantitative measurements of vibration amplitude using a contact-mode freestanding triboelectric nanogenerator. *ACS Nano* 8:12004–12013. <https://doi.org/10.1021/nn5054365>

- Xi Y, Zhang F, Shi Y (2021) Effects of surface micro-structures on capacitances of the dielectric layer in triboelectric nanogenerator: a numerical simulation study. *Nano Energy* 79:105432. <https://doi.org/10.1016/j.nanoen.2020.105432>
- Xiao TX, Jiang T, Zhu JX, Liang X, Xu L, Shao JJ, Zhang CL, Wang J, Wang ZL (2008) Silicone-based triboelectric nanogenerator for water wave energy harvesting. *ACS Appl Mater Interfaces* 10:3613–3613. <https://doi.org/10.1021/acsami.7b17239>
- Xu Y, Min G, Gadegaard N, Dahiya R, Mulvihill DMA (2020) unified contact force-dependent model for triboelectric nanogenerators accounting for surface roughness. *Nano Energy* 76:105067. <https://doi.org/10.1016/j.nanoen.2020.105067>
- Yamane C (2015) Structure formation of regenerated cellulose from its solution and resultant features of high wettability: a review. *Nord Pulp Pap Res J* 30:78–91. <https://doi.org/10.3183/npprj-2015-30-01-p078-091>
- Yamane C, Aoyagi T, Ago M, Sato K, Okajima K, Takahashi T (2006) Two different surface properties of regenerated cellulose due to structural anisotropy. *Polym J* 38:819–826. <https://doi.org/10.1295/polymj.PJ2005187>
- Yang Q, Fukuzumi H, Saito T, Isogai A, Zhang L (2011) Transparent cellulose films with high gas barrier properties fabricated from aqueous alkali/urea solutions. *Biomacromol* 12:2766–2771. <https://doi.org/10.1021/bm200766v>
- Yang J, Dahlström C, Edlund H, Lindman B, Norgren M (2019a) pH-responsive cellulose–chitosan nanocomposite films with slow release of chitosan. *Cellulose* 26:3763–3776. <https://doi.org/10.1007/s10570-019-02357-5>
- Yang W, Wang X, Li H, Wu J, Hu Y, Li Z, Liu H (2019b) Fundamental research on the effective contact area of micro-/nano-textured surface in triboelectric nanogenerator. *Nano Energy* 57:41–47. <https://doi.org/10.1016/j.nanoen.2018.12.029>
- Yin Y, Zhang C, Yu W, Kang G, Yang Q, Shi Z, Xiong C (2020) Transparent and flexible cellulose dielectric films with high breakdown strength and energy density. *Energy Storage Mater* 26:105–111. <https://doi.org/10.1016/j.jensm.2019.12034>
- Zhang R, Olin H (2020) Material choices for triboelectric nanogenerators: a critical review. *EcoMat* 2:e12062. <https://doi.org/10.1002/eom2.12062>
- Zhang R, Dahlström C, Zou H, Jonzon J, Hummelgård M, Örtengren J, Blomquist N, Yang Y, Andersson H, Olsen M, Norgren M, Olin H, Wang ZL (2020) Cellulose-based fully green triboelectric nanogenerators with output power density of 300 W m⁻². *Adv Mat* 32:2002824. <https://doi.org/10.1002/adma.202002824>
- Zhang R, Hummelgård H, Örtengren J, Andersson H, Olsen M, Chen W, Wang P, Dahlström C, Eivazi A, Norgren M (2023) Energy harvesting using wastepaper-based triboelectric nanogenerators. *Adv Eng Mat* 25:2300107. <https://doi.org/10.1002/adem.202300107>
- Zhou L, Liu D, Wang J, Wang ZL (2020) Triboelectric nanogenerators: fundamental physics and potential applications. *Friction* 8:481–506
- Zi Y, Niu S, Wang L, Wen Z, Tang W, Wang ZL (2015) Standards and figure-of-merits for quantifying the performance of triboelectric nanogenerators. *Nat Commun* 6:8376. <https://doi.org/10.1038/ncomms9376>
- Zou H, Zhang Y, Guo L, Wang P, He X, Dai G, Zheng H, Chen C, Wang AC, Xu C, Wang ZL (2019) Quantifying the triboelectric series. *Nat Commun* 10:1427. <https://doi.org/10.1038/s41467-019-09461-x>
- Zou H, Guo L, Xue H, Zhang Y, Shen X, Liu X, Wang P, He X, Dai G, Jiang P, Zheng H, Zhang B, Xu C, Wang ZL (2020) Quantifying and understanding the triboelectric series of inorganic non-metallic materials. *Nat Commun* 11:2093. <https://doi.org/10.1038/s41467-020-15926-1>

Publisher's Note Springer Nature remains neutral with regard to jurisdictional claims in published maps and institutional affiliations.